Micromachines **2014**, *5*, 27-49; doi:10.3390/mi5010027

OPEN ACCESS

micromachines

ISSN 2072-666X

www.mdpi.com/journal/micromachines

Review

Ultrasound-Induced Cell–Cell Interaction Studies in a Multi-Well Microplate

Martin Wiklund [1,*], Athanasia E. Christakou [1], Mathias Ohlin [1], Ida Iranmanesh [1], Thomas Frisk [1], Bruno Vanherberghen [1] and Björn Önfelt [1,2]

[1] Department of Applied Physics, KTH—Royal Institute of Technology, SE-106 91 Stockholm, Sweden; E-Mails: athachris@kth.se (A.E.C.); mathias.ohlin@biox.kth.se (M.O.); isir@kth.se (I.I.); tfrisk@kth.se (T.F.); brunov@kth.se (B.V.); bjorn.onfelt@ki.se (B.Ö.)

[2] Department of Microbiology, Tumor and Cell Biology, Karolinska Institute, SE-171 21 Stockholm, Sweden

***** Author to whom correspondence should be addressed; E-Mail: martin@biox.kth.se; Tel.: +46-8-5537-8134; Fax: +46-8-5537-8466.

Received: 19 December 2013; in revised form: 23 January 2014 / Accepted: 23 January 2014 / Published: 6 February 2014

Abstract: This review describes the use of ultrasound for inducing and retaining cell-cell contact in multi-well microplates combined with live-cell fluorescence microscopy. This platform has been used for studying the interaction between natural killer (NK) cells and cancer cells at the level of individual cells. The review includes basic principles of ultrasonic particle manipulation, design criteria when building a multi-well microplate device for this purpose, biocompatibility aspects, and finally, two examples of biological applications: Dynamic imaging of the inhibitory immune synapse, and studies of the heterogeneity in killing dynamics of NK cells interacting with cancer cells.

Keywords: ultrasound; lab-on-a-chip; acoustofluidics; acoustic trapping; natural killer cells

1. Introduction

Dynamic studies of single cells are important for our understanding of cell function and behavior [1]. Cells are complex biological systems that respond to different kinds of stimuli over time periods ranging from fractions of a second [2] to several days [3]. Even if the stimulus is kept constant in a certain measurement, the cellular response may vary over time and from cell to cell [4]. In standard bulk-based

assays, such variations are not resolved since the measured parameter is typically the average signal from many cells [1]. Thus, there is a need for screening methods where an individual cell's properties are measured. One such established and very efficient screening method is flow cytometry, or fluorescence-activated cell sorting (FACS) [5]. This method is based on a serial screening where fluorescence and/or scattered light are measured from individual cells at high throughputs. However, flow cytometry in its standard format is not compatible with dynamic monitoring, and therefore, only instantaneous cell properties are measured. On the contrary, live-cell fluorescence microscopy is a suitable tool for measuring dynamic cell properties [6]. Today, many different fluorescent probes exist for monitoring a variety of cellular functions, processes and status. Examples include live/dead assays, cell cycle assays and metabolic assays [7]. However, in order to combine both dynamic and single-cell monitoring, a tool for keeping track of each cell over time is needed. For this purpose, multi-well microplates can be used. In general, microplates have long been used in many different types of assays (e.g., in enzyme-linked immunosorbent assays (ELISAs)) [8]. However, in this review we focus on the use of microplates for live-cell microscopy imaging of individual cells [9].

When studying single cells in multi-well microplates, there are two different strategies that can be employed. One strategy is to dispense one cell per well for keeping track of each individual property of each single cell. This method has been used for e.g., single-cell culture and proliferation studies [10]. An alternative strategy is to dispense several cells per well and then to study individual interactions between two or more cells. This has been used for studying interaction between natural killer cells and different types and numbers of target cells [9,11–14], and also for migration studies [15].

Although microplates combined with live-cell fluorescence microscopy is a powerful tool for parallel and dynamic single-cell studies, it is still problematic when studying cell-cell interactions. The reason is that the time to cell–cell contact may vary depending on cell type, environment and microplate design [11]. In addition, there is a stochastic distribution in time to contact between different wells. This puts very high requirements on the imaging system and data analysis. Furthermore, it may also be of interest to study the effects of forced interaction and compare with spontaneous interaction. For these reasons, we have during the last few years developed and implemented ultrasonic particle manipulation technology into a microplate device designed for high-resolution live-cell fluorescence microscopy [16–18]. In this review, we summarize our work on the use of ultrasound as a tool for inducing and retaining cell–cell contacts in such multi-well microplates. The review discusses basic principles of ultrasonic manipulation technology and design criteria for such microdevices (Section 2), how to design a biocompatible manipulation system (Section 3), and finally an example of a biological application of the platform where the interaction between natural killer (NK) cells and cancer cells are studied (Section 4).

2. Method and Device

2.1. Method: Ultrasonic Manipulation of Cells

Ultrasonic manipulation of suspended particles is based on the time-averaged acoustic radiation force. This forces origins from a non-linear effect in the acoustic pressure field and was first described by Lord Rayleigh [19] and later nicely summarized in a review paper by Beyer [20]. In 1962, a very

useful theoretical model was presented by Gor'kov [21]. This model is valid for arbitrary sound fields and a single, spherical particle with known material properties. Gor'kov's generalized equation can be rewritten into the acoustic radiation force, **F**, dependent on the sound field, p and material properties [22]:

$$\mathbf{F}(p) = -\frac{V_p \beta_\mathrm{f}}{4} \nabla \left(f_1 p^2 - \frac{3}{2k^2} f_2 \left(\nabla p \right)^2 \right) \tag{1a}$$

with

$$f_1 = 1 - \frac{\beta_\mathrm{p}}{\beta_\mathrm{f}} \quad \text{and} \quad f_2 = 2\frac{\left(\rho_\mathrm{p} - \rho_\mathrm{f} \right)}{2\rho_\mathrm{p} + \rho_\mathrm{f}} \tag{1b}$$

here, p is the acoustic pressure amplitude, V_p is the volume of the particle, $\beta = 1/(\rho c^2)$ is the compressibility (defined by the density, ρ, and the sound speed, c), $k = \omega/c$ is the wave number, and f_1 and f_2 are the acoustic contrast factors defined by the compressibility β and the density ρ. The index "f" denotes "fluid" and the index "p" denotes "particle". From the equation, we conclude that the radiation force drives suspended particles in a direction parallel with the gradient of the acoustic field and has a direction and magnitude defined by the contrast factors f_1 and f_2. The magnitude is also dependent on the particle volume, V_p, and sound frequency (via $k = \omega/c$). Since steeper field gradients result in stronger forces, standing-wave fields are most often utilized. In a standing-wave field, the radiation force drives most suspended particles either to the pressure nodes or the pressure anti-nodes, depending on the signs of the contrast factors f_1 and f_2. In principle, particles stiffer than the suspension medium are driven to the pressure nodes (defined by the first term in Equation (1a)), while particles denser than the suspension medium are driven to the velocity antinodes (defined by the second term in Equation (1a)). In simple standing-wave fields (such as a one-dimensional field), the pressure nodes and the velocity antinodes are co-located. Although the standing-wave field in the multi-well plate is of more complex type, experimental observations confirm that the cells used in our work are driven to the positions of the numerically calculated pressure nodes [16].

When several particles are driven to a pressure node, they tend to aggregate in tight clusters. In one-dimensional (1D) standing-wave fields, the clusters typically take the form of flat monolayers in the pressure nodal planes. The reason for this is the particle-particle interaction force, sometimes called the Bjerknes force [23]. However, in 2D or 3D standing-wave fields, the cluster shapes are more complicated to predict or control [24].

The theoretical model above (Equation (1)) is valid for spherical particles with well-known material properties (density and compressibility) suspended in an inviscid fluid. However, the method reviewed in this paper is designed for cell applications. Generally, cells have unknown material properties, or if known, their material properties have a wider distribution than for synthetic particles (e.g., polystyrene). In addition, the material properties of cells are also dependent on many external and internal factors. Altogether, this makes it difficult to predict the contrast factors f_1 and f_2 for cells. Nevertheless, attempts have been made to estimate the contrast factors and corresponding radiation forces acting on different cell types. For example, Barnkob *et al*. [25] used two types of particles (polystyrene and melamine resin) for calibrating the radiation forces from a known acoustic field, and used this data for measuring the contrast factors for two different cell types: White blood cells and DU145 prostate cancer cells. They concluded that the radiation force was about one order of magnitude smaller for these cells, relative

polystyrene particles of equal size. A similar approach was carried out by Hartono *et al*. [26], who concluded that the radiation force was 1.5 times smaller for red blood cells, and between 2 and 4 times smaller for different types of cancer cells relative to the force on equally sized polystyrene. Furthermore, Mishra *et al*. [27] concluded from numerical modeling that for biological cells, the radiation force was less dependent on shape but more dependent on internal structures and inhomogeneity. For example, the force on a cell with nucleus was predicted to be approx. twice the force of a non-nucleated cell of similar size. In summary, we may expect the acoustic radiation force in a given acoustic field to be roughly a few times smaller for cells than for polystyrene particles of similar size, and that the corresponding trapping time is expected to be a few times longer.

2.2. Device: Ultrasonic Manipulation in a Multi-Well Micro-Plate

For the design of the multi-well microplate used for ultrasonic cell manipulation, the following criteria have been prioritized [12]: The microplate should be compatible with high-resolution optical microscopy, and it should be biocompatible allowing long-term cellular assays. In addition, it should also be easy to use by a non-technically skilled operator. An illustration of the microplate fabrication process is shown in Figure 1. A complete description of the fabrication process is given in Ref. [12]. In summary, silicon wafers with diameter 100 mm and thickness 300 μm (Figure 1a) were used for processing of nine individual microplates per wafer, where each final microplate is 22 × 22 mm^2 (Figure 1h). Each microplate has 10 × 10 wells, where each well is 300 μm deep and with horizontal cross section 300 × 300 μm^2, or 350 × 350 μm^2, and with 100 μm wall thickness between individual wells. After spinning photo resist on the silicon wafer (Figure 1b) and defining the well geometry by lithography (Figure 1c), the wells were etched through the 300 μm silicon layer by deep reactive-ion etching (DRIE) (Figure 1d). Care was taken to optimize the process so that the wells had a constant cross section through the depth of the silicon layer. This was confirmed by scanning electron microscopy (SEM) after the etching process and with a silicon layer that was diced across the wells [12]. Following the deep-etching of the wells and stripping of the photo resist and oxide mask (Figure 1e), the silicon wafers were furnace wet-oxidized to a surface oxide thickness of approx. 200 nm (Figure 1f). This important step was performed for improving the biocompatibility [12], and also for enabling cleaning and re-usage of the microplates. Finally, a 175 μm thick borosilicate glass layer was anodically bonded to each processed silicon layer (Figure 1g), and the silicon-glass stack was diced into square-shaped microplates (Figure 1h).

Two different designs have been used for the ultrasonic actuation system for the microplates. The original design [16,18] used a wedge-transducer [22,28] (Figure 2a). In the upgraded version of the ultrasonic actuation system, the wedge transducer was replaced by a ring transducer, which was fully integrated into the microplate holder [17] (Figure 2b). This device is more robust and simple to use, but requires higher driving voltages. The wedge-transducer device (Figure 2a) consists of an ultrasonic transducer made by a piezoceramic plate (1) and a titanium wedge (2). The transducer is positioned on top of the multi-well microplate (5), and it is reversibly glued with a thin layer of water-soluble adhesive gel. The cell suspension sample is pipetted from above over the wells and stored within a rectangular frame made in PDMS (4), which can be closed by a glass cover slip (3) to minimize evaporation. The other device, the ring-transducer chip (Figure 2b), has the same general function including

parts (3)–(5), but here the ultrasonic coupling is accomplished from below via a larger ring-shape piezoceramic plate (6). This design is more robust and reliable since it is not dependent on how the transducer is positioned relative to the chip. Furthermore, it is also more temperature-stable when driven at higher voltages (>20 Vpp) and therefore more suitable for applications requiring higher radiation forces, faster response times and long assay times (up to several days). Both designs shown in Figure 2a,b are relatively broadband, which is useful for the employed ultrasonic actuation method described below.

Figure 1. Schematic outline of the silicon-glass microplate fabrication process. (**a**) Oxidized silicon wafer, 100 mm in diameter, 300 μm thick; (**b**) Spin coating of wafer with positive photoresist; (**c**) Masked UV-exposure of photoresist layer; (**d**) Plasma etching of the oxidized silicon wafer; (**e**) Removal of photoresist and oxide mask; (**f**) Oxidation of the wafer after the strip of the photoresist and oxide mask; (**g**) The anodic bonding of the 175 μm thick glass bottom to the silicon "grid"; (**h**) Dicing to individual chips, 9 per wafer, where each final chip is 22 × 22 mm^2. Based on a figure in Ref. [12].

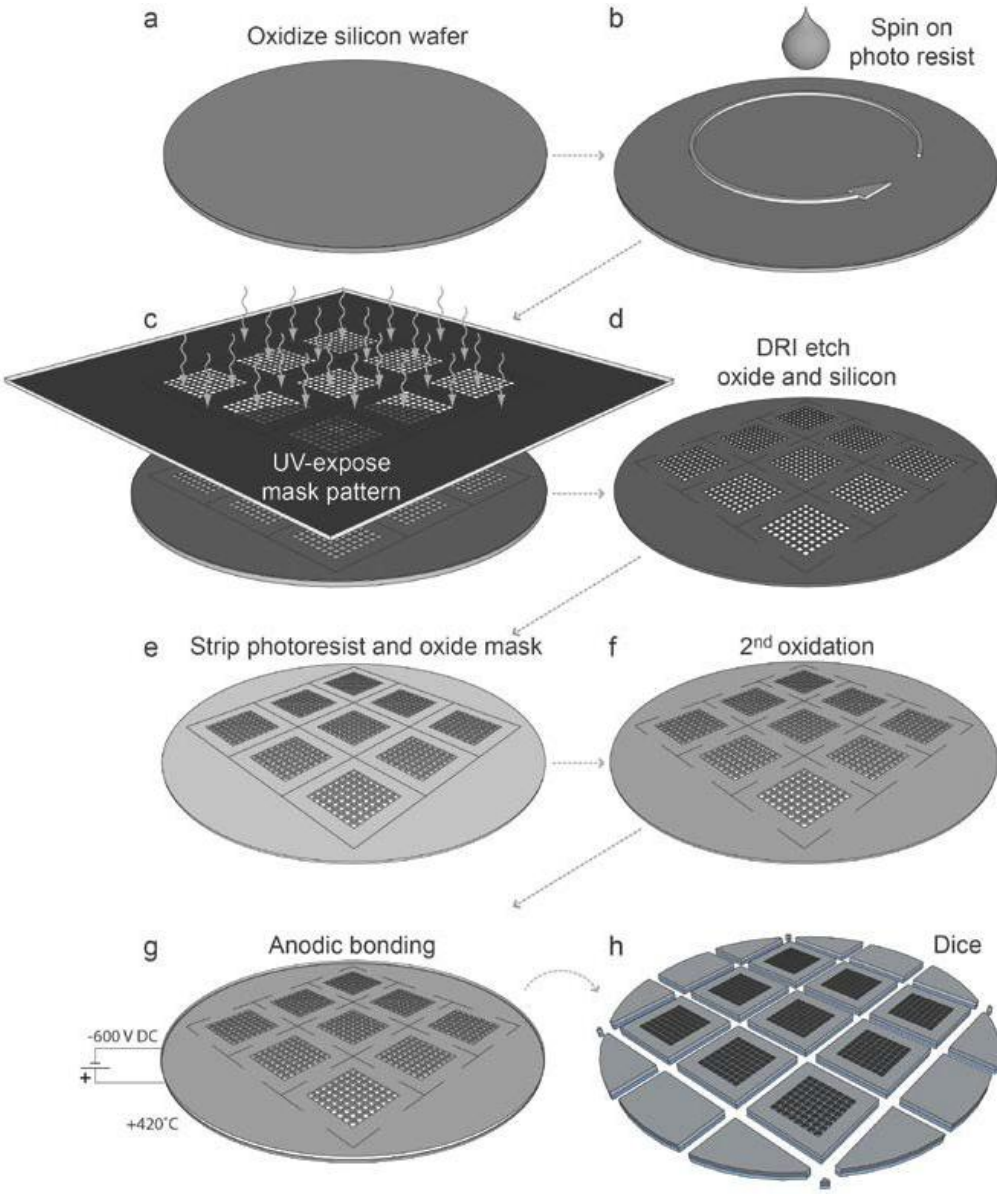

Figure 2. The two different designs of ultrasonic actuation system used for the multi-well microplate: The wedge-transducer device [18] (**a**) and the ring-transducer device [17] (**b**). (1) Piezoceramic plate; (2) Titanium wedge; (3) Glass lid; (4) PDMS frame; (5) Multi-well microplate; (6) Ring-shaped piezoceramic plate.

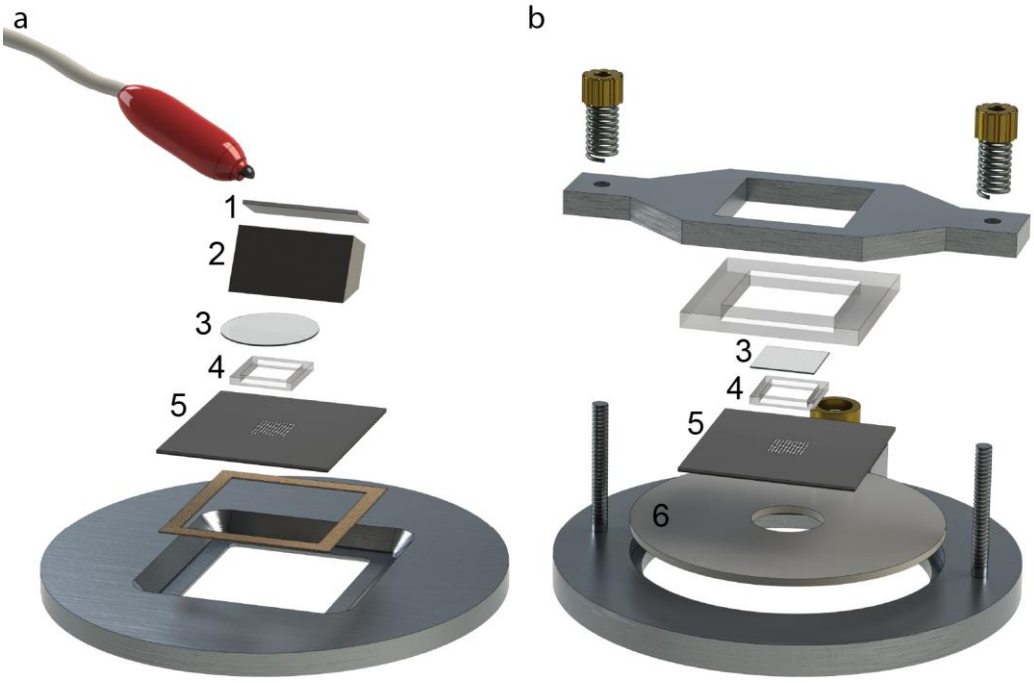

The purpose of the ultrasonic actuation in the multi-well microplate is to create an acoustic resonance in each well, so that suspended particles or cells are aggregated and positioned by the acoustic radiation force described by Equation (1). The trapping position is in most cases the pressure node of the standing wave formed in the fluid cavity (*i.e.*, the well) by the acoustic resonance. In a two-dimensional rectangular cavity with dimensions L_x and L_y, the acoustic pressure, p, is described by [29]:

$$p(x,y,t) = p_0 \cos(k_x x)\cos(k_y y)\sin(\omega t) \tag{2a}$$

$$k_x = \frac{n_x \pi}{L_x}; \quad k_y = \frac{n_y \pi}{L_y} \tag{2b}$$

where k_x and k_y are the wavenumbers for each horizontal direction (x and y) in the cavity, and n_x, $n_y = 0, 1, 2, 3, \ldots$, are the numbers of half wavelengths along the x- and y-directions, respectively. Note that in Equation (2), we have neglected any (vertical) z-dependence of the pressure. In practice, this is valid for three-dimensional cavities having short L_z-dimensions (relative the acoustic wavelength). Given an acoustic resonance in the fluid cavity described by Equation (2), the resonance frequency of mode (n_x, n_y) is [29]:

$$f_{(n_x,n_y)} = \frac{c}{2\pi}\sqrt{k_x^2 + k_y^2} = \frac{c}{2\pi}\sqrt{\left(\frac{n_x \pi}{L_x}\right)^2 + \left(\frac{n_y \pi}{L_y}\right)^2} \tag{3}$$

where c is the sound velocity in the fluid. If the purpose is to trap the particles in the center of each well, one should use the lowest possible resonance mode. The wells used in our multi-well microplate have

square-shaped horizontal cross-sections (*cf.* Figures 1, 3 and 4). For a square-shaped cavity ($L_x = L_y$), the lowest possible mode is either the (1,0)-mode or the (0,1)-mode. According to Equation (3), these two modes have identical frequencies, and it is therefore not clear how the pressure field can be described at this frequency. However, due to differences in boundary conditions and properties/shapes of the supporting structures around the wells, the two modes are often slightly degenerated. Thus, for a given excitation frequency, only one of the two modes exists. In our multi-well microplate, where a complex acoustic interaction between all 100 wells occurs, the result is a pressure field inside each well having a node oriented as shown in the simulated pressure field in Figure 3a (and described more thoroughly in Ref. [16]). As seen from the simulation, the node of the half-wave resonance in each well is not a pure (1,0)- or (0,1)-mode, but rather something in between. If the excitation frequency is slightly changed, the node orientation changes (primarily it rotates). For this reason, a simple method for generating point-shaped pressure nodes in the center of each well is to quickly average a set of such single-frequency resonances. We have realized this by cycling linear frequency sweeps around the nominal (1,0)- or (0,1)-resonance frequency. The simulation result of this frequency modulation scheme is shown in Figure 3b. The simulated acoustic resonances in Figure 3a,b are experimentally confirmed using the wedge-transducer device in Figure 3c,d, respectively. Here, the pressure field is visualized by the shapes and positions of 5 μm polyamide particle aggregates driven to the pressure nodes by the acoustic radiation force. Experimentally, frequency modulation actuation is realized by sawtooth-modulation with a center frequency corresponding to the (1,0) or (0,1) resonance (which is around 2.5 MHz for a 300 × 300 μm^2 well) and a typical bandwidth of 100 kHz and a cycling rate of 1 kHz. This modulation function is very simple to implement since it is a built-in function in most signal generators. The modulation bandwidth is difficult to predict theoretically and needs instead to be optimized experimentally for each microplate device. The cycling rate is typically chosen as a rate being above the threshold for aggregate movement (*i.e.*, time for reconfiguration of the aggregate between different single- frequency resonances within the sweep). We have concluded that a rate of 1 kHz is well above this threshold. Finally, a similar experimental verification for the ring-transducer device is shown in Figure 4. Here, we used a microplate with well size 350 × 350 μm^2 actuated with center frequency 2.30 MHz and modulation bandwidth of 200 kHz. When using a lower concentration of 10 μm particles, it is clear from the experiments that particle trapping and aggregation work for both single-frequency actuation (blue aggregates) and frequency-modulation actuation (red aggregates). However, the accurate positioning of aggregates in the center of each well can only be accomplished by frequency-modulation actuation. In addition, frequency modulation also provides more compact aggregates [17].

A limiting factor for the trapping performance in any acoustophoretic device is acoustic streaming [30]. In the multi-well microplate, acoustic streaming causes the trapped particles or cells to be flushed away upwards if very high actuation voltages are used (approx. 100 Vpp or more) [17]. One reason for this streaming is that it is not an accurate approximation to model the wells in the microplate as 2D cavities (*cf.* Equations (2) and (3)). Thus, Equations (2) and (3) are useful for qualitative understanding of how resonances are built up in the system and for predicting trapping positions of cells, but for accurate quantitative modeling including acoustic streaming, a 3D model is needed. This is a challenge for future work. Still, it should be mentioned that the frequency-modulation methods tends to suppress acoustic streaming when comparing with single-frequency actuation [30,31]. Thus, for moderate actuation

voltages using the frequency modulation method, acoustic streaming is not causing any problem for the trapping efficiency and trapping stability over time.

Figure 3. Comparison between modeling (**a**,**b**) and experiments (**c**,**d**) for the wedge-transducer device. Simulation of the time-averaged pressure squared (p^2) for single-frequency actuation at 2.60 MHz (**a**) and for the average of 50 single frequencies between 2.55 and 2.65 MHz (**b**). Both plots are normalized individually and shown in logarithmic scale. The predicted trapping locations (*i.e.*, the minima of p^2) are indicated in yellow (in **a**) and in dark blue (in **b**). Experimental confirmation of the simulations using 5 µm particles at single-frequency actuation (**c**) and with frequency-modulated actuation (**d**) using the same frequency intervals as (**a**) and (**b**). Scale bar is indicated by the wells (300 µm wide squares).The figure is reproduced from Ref. [16] with permission from RSC.

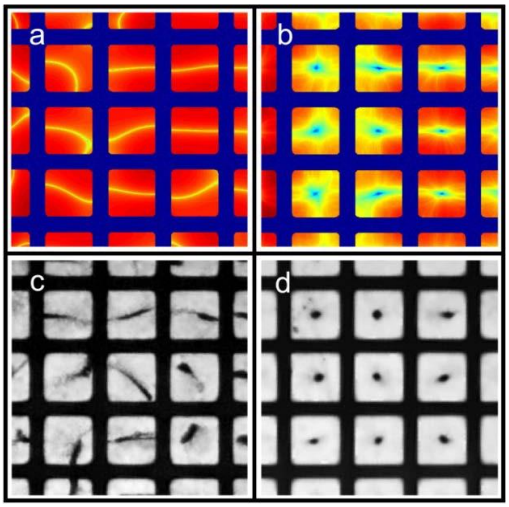

Figure 4. Detailed experimental evaluation of the trapping and positioning performance of 10 µm particles in the ring-transducer device. Scale bar is indicated by the wells (350 µm wide squares with slightly rounded walls). The actuation frequency is 2.30 MHz (single-frequency, blue aggregates) and 2.30 ± 50 kHz at the modulation rate 1 kHz (frequency-modulation, red aggregates). The figure is based on results presented in Ref. [17].

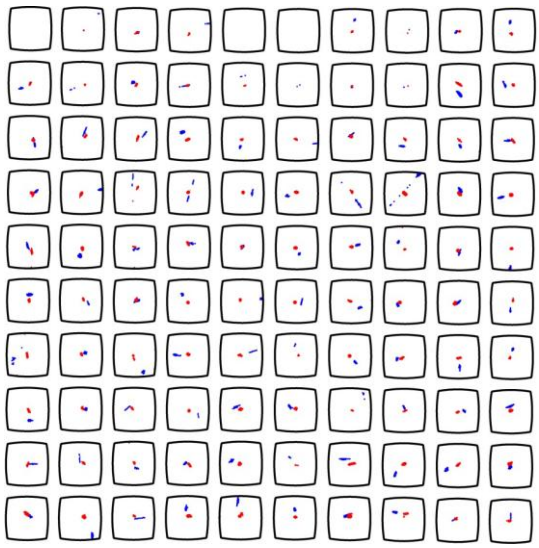

For the practical handling of the device with a cell suspension sample, the method is summarized in Figure 5. The fluid reservoir within the PDMS frame shown in Figure 5a has the purpose of providing a controlled environment of temperature- and CO_2-regulated cell medium. The cell medium volume (50 μL) needs to be large enough for enabling cell culturing over long terms (hours to days) and also for the practical handling (*i.e.*, enough to avoid sample evaporation). To this primed volume of cell medium, a small aliquot of cell suspension is pipetted from above (see Figure 5b) before closing the device with the glass lid (*cf.* item #3 in Figure 2). The seeding of cells into the wells is based on gravitational settlement (see Figure 5c). The strength of this method, besides simplicity, is the ability to study different numbers of cells per well interacting. Thus, the average number of cells per well is controlled by the cell concentration in the added drop (*cf.* Figure 5b), and the seeding principle causes a stochastical distribution around this average. Finally, when ultrasound is applied with the frequency-modulation method presented in Figure 3, the cells are aggregated and positioned in the center of each well where they can be monitored over time by high-resolution fluorescence microscopy. If confocal microscopy is used, it is a benefit to know the exact locations of the 100 cell aggregates. Since confocal microscopy is a relatively slow method, only the small area where the cells are located needs to be scanned, instead of the whole microplate.

Figure 5. Schematic illustration (not to scale) of the different steps of the cell handling method. For simplicity, only three out of a hundred wells are shown (vertical cross-section view), and only the PDMS frame and the multi-well microplate (item #4 and #5 in Figure 2). (**a**) The microplate is first primed with cell medium shown in blue; (**b**) The cell suspension is added as a small drop from a pipette tip; (**c**) Cells sediment by gravity down into the wells. The average number of cells per well is controlled by the cell concentration in the added drop in (**b**). In this example, there is on average 1 red cell and 2.33 green cells per well; (**d**) When ultrasound is turned on according to the procedure described in Figure 3, cells are trapped, aggregated and centrally positioned in each well.

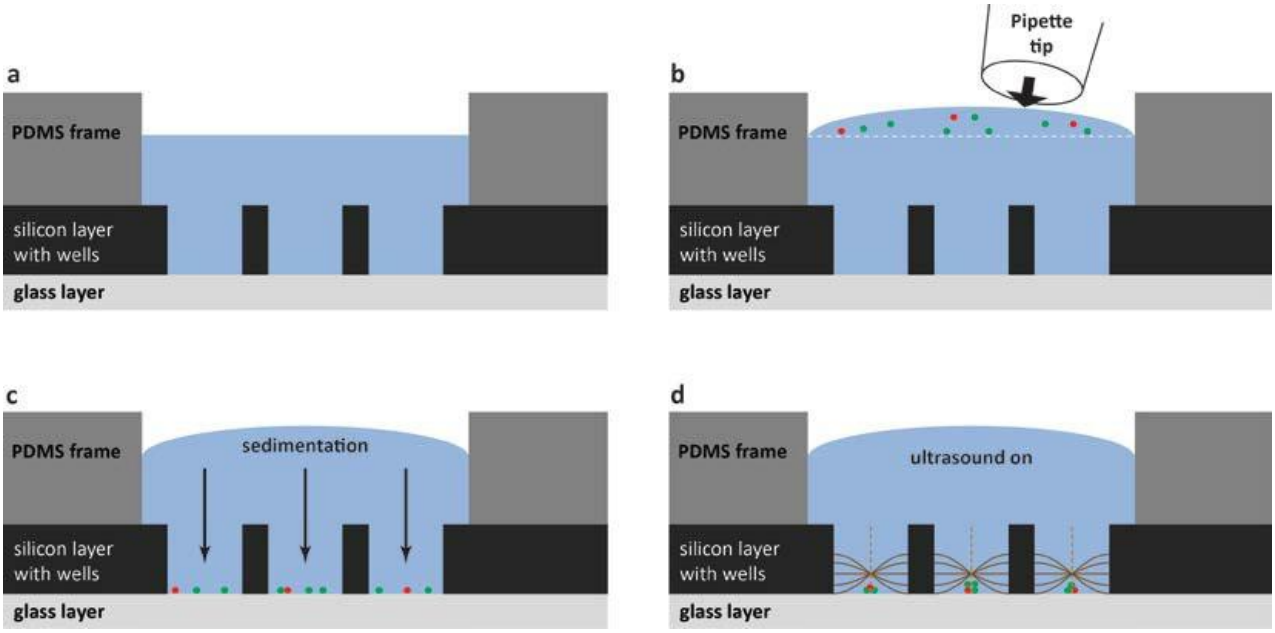

2.3. Quantifying Acoustic Energy Density, Acoustic Pressure Amplitude, Acoustic Radiation Forces and Acoustic Streaming

In order to fully characterize the device, it is important to be able to measure the properties of the acoustic field including the acoustic radiation forces and acoustic streaming acting on the particles, cells and the fluid, respectively. In a resonant acoustic field, there is no clear propagation direction of the wave. For that reason, acoustic energy density is a commonly used measure. This energy density can be translated into, e.g., acoustic pressure amplitude or acoustic radiation force (*cf.* Ref. [17]). Thus, knowing these acoustic field properties is important for estimating the trapping efficiency of cells, but also for estimating the risk of having cavitation in the sample (see Section 3). It is very difficult to measure the acoustic field properties by direct methods in an acoustofluidic device. However, there are different indirect methods available. Here, we will present three different methods used in our lab: Light intensity, particle tracking and particle image velocimetry (PIV). The methods are based on translating a measured property (i.e., light intensity, particle position or particle velocity) into acoustic energy density or acoustic pressure. All methods are based on one-dimensional (1D) geometries, but can be used for 2D geometries for order-of-magnitude estimations of the energy, pressure and forces.

The first method, light intensity, has been developed in collaboration with Rune Barnkob and Henrik Bruus (Denmark Technical University, Copenhagen, Denmark) [28,32]. This method is specifically designed for acoustofluidic chips that are optically transparent and compatible with standard bright-field microscopy [6]. One strength of the light intensity method is that the chips do not need to be compatible with high-resolution microscopy. For example, individual particles do not need to be resolved, and relatively high particle concentrations (up to 10^9 beads/mL) can be used. In brief, the method is based on measuring the total transmitted light intensity passing through a certain part of a microchannel or a microchamber during the focusing process of suspended particles. When particles are focused and trapped in the pressure node, the fluid cavity gradually becomes more transparent for light. A detailed description of the method is found in Ref. [32], but here it is sufficient to show an example of what the method can be used for. In Figure 6, we demonstrate quantification of the acoustic energy density in a microchannel when it is operated at a single (optimal) frequency, and we compare with the corresponding energy density for the same (center) frequency, but with the frequency-modulation function active (100 kHz bandwidth and 1 kHz rate). As seen in the diagram, the average energy density is just slightly lower for frequency-modulation relative single-frequency actuation. This result is important since it means that there is no compromise between positioning accuracy and radiation forces when using frequency- modulation actuation instead of single-frequency actuation.

Another relatively simple and straightforward method for measuring acoustic energy density is particle tracking. This method is based on either manual or automated tracking of the position of individual particles over time. Thus, the method requires well-resolved particles and moderate particle concentrations (i.e., no particle-particle overlaps in the recorded images). The tracking data from a time sequence following a particle from its initial position into the pressure node can then be translated into a radiation force based on balancing Equation (1) with the viscous drag [17]. This method has been used for, e.g., measuring the quality factor (*Q*-value) of an acoustophoretic resonance in a microdevice by measuring the energy density as a function of the actuation frequency [33]. For the multi-well microplate discussed in this review, particle tracking was performed for estimating the forces acting on

10 μm polystyrene particles in the wells. The particle tracks in one of the hundred wells are shown in Figure 7 (six repetitions of the same experiment). This data containing tracks of 30 particles resulted in an acoustic energy density between 1 and 4 J m^{-3}, which corresponds to acoustic pressure amplitudes of 0.3–0.7 MPa, and acoustic radiation forces from 10 to 50 pN. These values are within the range of biocompatible ultrasonic manipulation of cells [34].

Figure 6. Measurement of the spatial distribution of the acoustic energy density along a micro-channel (*x*-axis), when actuating the chip with (**a**) Single-frequency (SF) actuation; and (**b**) Frequency-modulation (FM) actuation. The light-intensity method was applied to eight 150 μm wide subsections of the recorded images. The averaged energy density for the whole channel, $E_{ac,avg}$, is marked with a dotted black line, and the corresponding 1σ standard deviation is marked with a grey band. The red error bars are the standard deviations from the four repetitions of each experiment. The figure is reproduced from Ref. [28] by permission from IOP Publishing.

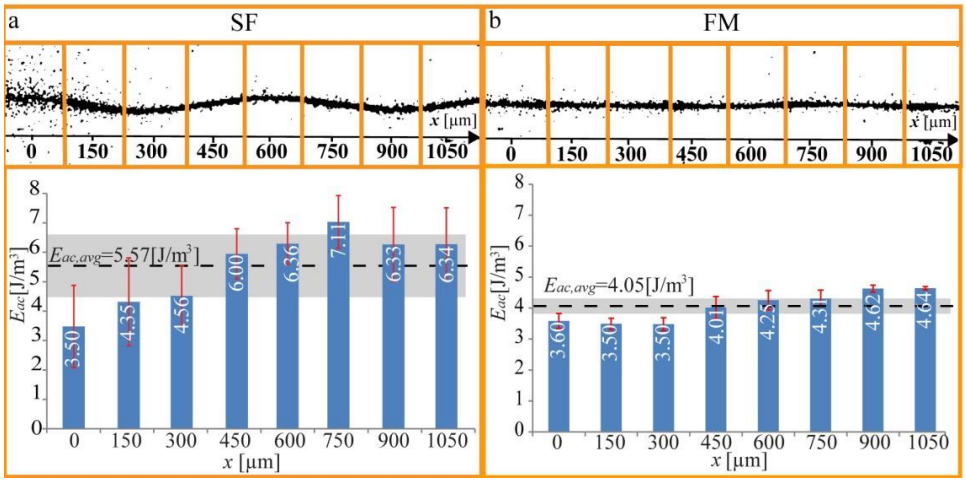

The last method, particle image velocimetry (PIV) [35], analyzes groups of particles from recorded image sequences, rather than individual particles (as for the particle tracking method). When applied to a microsystem using a microscope, the method is often called micro-PIV. The group of particles to be analyzed is defined by a certain interrogation window in the recorded image. Two such corresponding interrogation windows from two image frames separated in time are then inserted into a cross-correlation algorithm that compares light intensities for generating a velocity vector. The full velocity vector field can be used in the same way as for the particle tracking method for calculating the acoustic radiation forces. A strength of PIV is that it allows automated analysis of complex velocity fields. However, it is a time-consuming procedure to acquire reliable PIV data [36].

It is also possible to use PIV for measuring acoustic streaming in a microfluidic device. This has been performed in the multi-well microplate together with the particle tracking method described above. Thus, acoustic radiation forces and acoustic streaming velocities can be measured simultaneously when the two methods are combined. This is shown in Figure 7, where the background velocity field is measured by micro-PIV using 1 μm polystyrene beads [17]. The reason that the two methods can be combined is that the 10 μm particles are less influenced by acoustic streaming, and 1 μm particles are less influenced by the acoustic radiation force at the utilized frequency range (2–3 MHz) [37].

Figure 7. Particle tracking for estimation of acoustic radiation forces acting on 10 µm polystyrene particles, and particle image velocimetry (PIV) diagrams showing the background velocity field from acoustic streaming. The diagrams show the particle motion in the same well for six repetitions of the experiment after re-seeding the well with new particles. The tracks of 10 µm particles are indicated by circles (one color per individual particle), and the acoustic streaming is measured by with 1 µm particles used as flow trackers. The diagrams are based on a figure in Ref. [17].

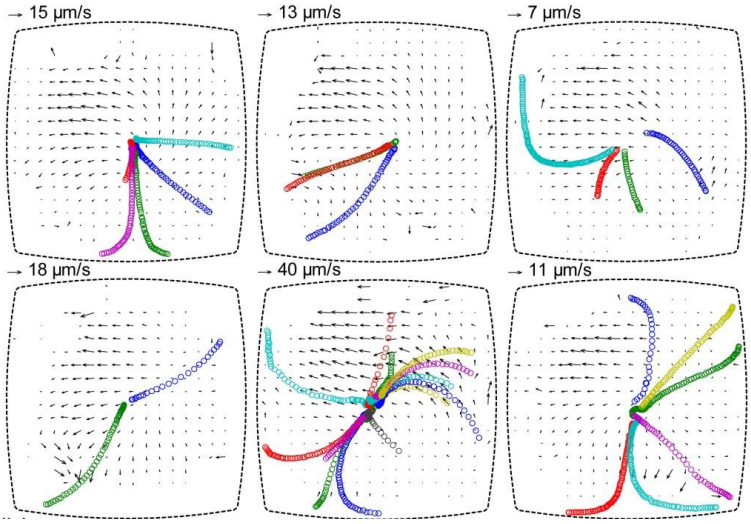

It is interesting to compare the three methods (light intensity, particle tracking and PIV). Light intensity has the advantage that it can be used with high particle concentrations and limited optical performance of the microscope. It does not require any advanced equipment or skillful operator, and can therefore easily be implemented in any lab. However, an optically transparent chip is needed [28,32]. The next method, particle tracking, is also easy to implement and it is the most suitable method for measuring the local pressure amplitude without any possible disturbance from particle-particle interactions. (Note that all three methods utilize the Gor'kov equation (Equation (1)) which assumes single particles.) However, particle tracking is time-consuming and provides low spatial resolution of the measured energy density. Finally, PIV is the most sophisticated method and can, if performed properly, provide very accurate and reliable data [36]. However, PIV requires careful tuning of the particle concentration and image properties of the microscope, relative the input parameters in the PIV algorithms (primarily the size of the interrogation window defining the spatial resolution of the measure field). Therefore, a PIV-trained operator is needed.

3. Biocompatibility

3.1. Effect of Ultrasound on Cell Viability and Function

The multi-well microplate is designed to be used for dynamic cell-cell interaction studies by combining ultrasonic trapping and live-cell fluorescence microscopy. This means that the cell-cell interactions are monitored in real-time over time periods lasting from minutes to several days. For this reason, it is of outmost importance that the ultrasound is not causing any harm or interferes with the studied biological process of interest. A more detailed review about biocompatibility of acoustofluidic

microdevices is found in Ref. [7]. In brief, the bioeffects of ultrasound techniques for different medical or biomedical applications can differ a lot. For example, diagnostic ultrasound imaging, that uses similar frequencies and energies as in ultrasonic cell manipulation, is today considered as one of the safest imaging methods, and is widely used in clinics around the world. On the other hand, ultrasound can also be used for the purpose of specific destruction of biological material. Examples include shock-wave lithotripsy and high-intensity focused ultrasound (HIFU), where ultrasound is used for, e.g., destroying kidney stones and gall stones.

When using ultrasound for cell manipulation in a microdevice, the two most important parameters to control in terms of biocompatibility are the temperature and the pressure amplitude [7]. The ultrasound may cause heating of the cell sample, and high pressure amplitudes may lead to cavitation. Concerning temperature, the most common sources of heating in an acoustically driven micro-device are losses in the piezoceramic plate, and absorption in lossy supporting structures such as glue layers and polymer-based layers. It is an advantage to minimize the size and amount of such layers. The other parameter of importance for the biocompatibility is the pressure amplitude, which has relevance for the risk of having cavitation in the fluid. Generally, cavitation can be defined as the formation and/or activity of gas/vapor filled cavities, i.e., bubbles, in a fluid medium. Here, ultrasound is one out of many means to initiate and drive cavitation [7]. This stimulated bubble activity leads to local fluid jets causing shear stresses on cells and high local pressures and temperatures that can lead to direct cell death. Although cavitation is primarily associated with low-frequency ultrasound (e.g., "sonication" at 20–50 kHz), it can still be initiated even at MHz-frequencies typically employed for ultrasonic manipulation of cells. The threshold for initiating cavitation is dependent on frequency, pressure amplitude, but also on the size of potential pre-existing bubbles in the fluid. The latter is of high importance, and care should be taken to degas the fluid medium properly before injecting it to the chip. The acoustic pressure amplitudes used in the multi-well microplate (up to 0.7 MPa at 2.5 MHz actuation) are safe given that the fluid does not contain any gas bubbles with sizes of the order of 1 μm. If such bubbles should exist, the cavitation threshold could in theory be as low as 0.4 MPa at 2.5 MHz actuation [38].

In order to optimize biocompatibility of the multi-well microplate, we place the device in an environmental chamber matching the microscope stage where temperature and CO_2-level are controlled around 37 ℃ and 5%, respectively [16,18]. These values are the same as in a standard cell culture incubator. Furthermore, we use temperature probes (thermocouples) positioned as close to the fluid chamber as possible, in order to confirm that the ultrasound is not causing any temperature elevation above 37 ℃. If so, the set-point temperature of the environmental chamber needs to be lowered with the same amount as the ultrasound-induced temperature increase. For estimating the risk of having cavitation, the pressure amplitude in the wells can be calibrated by the use of the particle tracking method described in Section 2.3. In a recent paper by Ohlin *et al*. [17], the highest measured pressure amplitude in the ring-transducer microplate was 0.7 MPa. This was measured for an actuation voltage approx. one order of magnitude higher than used during normal operation of the device with cells [16,18]. This means that cavitation is in practice impossible during normal operation of our device.

3.2. Measuring Cell Viability and Function with Optical Microscopy

Although we can control heating and avoid cavitation, it is still important to measure the cell viability and cell functions when the cells are exposed to ultrasound for prolonged times. Our first study was performed by Hultström *et al*. [34], who measured the viability and proliferation rate of adherent monkey kidney cells (COS-7) at different ultrasound exposure times. Here, the viability was monitored during the ultrasound exposure by the viability probe calcein-AM, and the proliferation rate was quantified by measuring the cell doubling time after ultrasound exposure. We concluded that exposure times up to 75 min at 0.85 MPa pressure amplitude and 3 MHz frequency did not alter viability or change the expected cell doubling time (24–48 h). Instead, the control cells not exposed to ultrasound showed lower doubling times, potentially because they were not first aggregated as for the ultrasound-exposed cells. Thus, it is reasonable to believe that the cell-cell contact induced by the ultrasound could be beneficial for cell proliferation of adherent cells. In a follow-up study, Vanherberghen *et al*. [16] used the multi-well microplate for studying the viability and proliferation of immune cells (a calcein-AM-labeled B cell line). Here, we concluded that the ultrasound (similar amplitudes and frequencies as in the previous study) did not cause any noticeable effect on B cells exposed to ultrasound continuously for up to three days (see Figure 8).

Figure 8. B cells growing in the multi-well microplate driven with the wedge transducer continuously at 10 V_{pp}, 2.5 MHz (frequency modulation) for 60 h. The figure is based on results presented in Ref. [16].

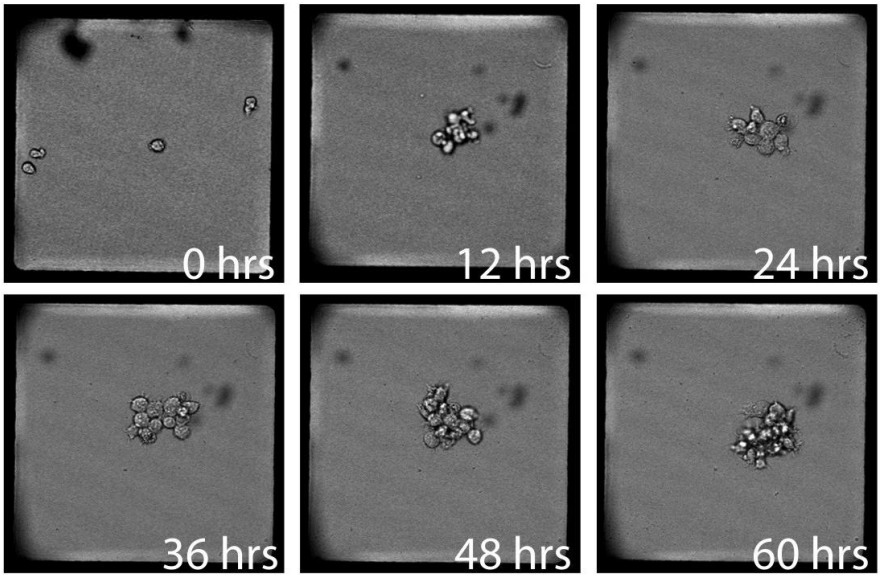

Besides viability and proliferation, it is important that the cell functions are intact when the cells are exposed to ultrasound. Several studies have been performed where different cell types and cell functions have been investigated after short-term ultrasound (seconds to minutes). For example, Augustsson *et al*. [39] and Burguillos *et al*. [40] used the XTT assay for measuring the mitochondrial dehydrogenase activity present in cells from prostate cancer cells and BV2 microglial cells, respectively. In another study, Bazou *et al*. [41] performed different biochemical assays on HEP-G2 liver cell aggregates (e.g., detection of hypoxia, cytokeratin-18, glucose and lactate). In the following section (Section 4), we

investigate the functions of natural killer (NK) cells interacting with different target cells during long-term ultrasound exposure. Besides viability and proliferation, we have studied the ability to form immune synapses and the ability of NK cells to selectively kill different target cells.

4. Natural Killer (NK) Cell—Cancer Cell Interaction Studies

NK cells are lymphocytes of the immune system and they serve the role of cytotoxic effector cells against virus-infected or cancerous cells as well as cytokine producers for triggering other immune responses. NK cells are characterized by the capability of direct killing of aberrant cells through release of cytotoxic granular content (e.g., perforin and granzymes) at the tight intercellular contact (called "immune synapse" or sometimes "immunological synapse") formed between the NK cell and target cell [42]. The immune synapse was initially described as the junction between T helper lymphocytes and antigen presenting cells (APC) where T cell receptors (TCRs) are interacting with major histocompatibility complex (MHC) molecules on APC carrying foreign or malignant peptides [43,44]. Some viruses have developed mechanisms to suppress the expression of MHC proteins at the cell surface, effectively hiding any virus-associated antigenic peptides and therefore avoiding recognition by T cells. However, NK cells express a range of activating and inhibitory cell-surface receptors that are used to probe the "health" status of potential target cells. Reduced levels of MHC in combination with activating signals can trigger delivery of granules to the immune synapse followed by granule content release that will initiate a signaling cascade inside the target cells, which eventually leads to apoptosis. In an immune synapse dominated by inhibitory signals NK cells will eventually detach leaving the target cell unharmed [45]. The outcome of the immune synapse depends on a balance between activating and inhibitory signals mediated by receptor-ligand interactions at the NK-target interface. The two different outcomes described here, inhibition and activation, are schematically illustrated in Figure 9a,b, respectively.

Figure 9. Schematic illustration of an inhibitory (**a**) and an activating (**b**) interaction between a natural killer (NK) cell and a target cell. The three different steps (marked with arrows) are (I): Initiation of cell-cell contact, (II): Development of an inhibitory (green) or activating (red) immune synapse, and (III): Detachment (**a**) or killing (**b**) of the target cell. The ultrasound is used for synchronizing step I in all wells simultaneously (*i.e.*, synchronizing $t_{contact}$) and for retaining the cell-cell interaction from step I to step III.

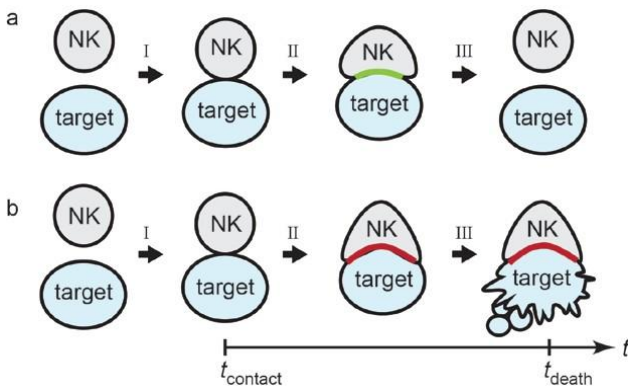

Conventional methods of investigating NK cell properties and functions (such as 51Cr release cytotoxicity assay) are based on bulk averages that hide information related to characteristics of

individual NK cells. High NK heterogeneity has been shown by experiments performed on human [46,47] and mouse [48] NK cells indicating the need of more efficient, high throughput and well controlled techniques for single cell analysis. With the multi-well microplate device presented in the previous sections, we can induce synchronized NK-target cell interactions in parallel. Our method allows imaging of isolated events within the individual wells. Thus, we are able to observe and record up to one hundred individual interactions between NK cells and target cells and the resulting NK responses within a specific time frame depending on the experiment [18]. Furthermore, current high-resolution imaging techniques are limited by the tendency of cells to migrate or drift away from the imaging area (field of view). We have shown that besides inducing cell-cell contact and thus initiation of the interaction, we can also maintain the cell conjugates within a well-controlled area in each well allowing high resolution confocal imaging [18].

As mentioned in Section 3, we are able to maintain appropriate cell environmental conditions during the entire experiments performed in the microplate-microscope setup. In addition, we have quantified the trapping performance of the device for two cell types with different adherent properties. The human embryonic kidney cell line 293T with adherent properties were poorly trapped compared to the suspension B cell line 721.221. This strongly indicates that acoustic forces applied on the cells are balanced to natural biological forces such as cell adherence to a glass substrate.

4.1. High-Resolution Imaging of the Inhibitory Immune Synapse

In our recent study [18] a human NK cell line (YTS) transfected to express the inhibitory NK cell receptor KIR2DL was imaged while interacting with a human B cell line 721.221, deficient in endogenous surface expression of MHC class I proteins and transfected to express MHC/HLA-Cw6 (cognate ligand to KIR2DL1) coupled to green fluorescent protein (GFP). Accumulation of GFP (green color) in the immune synapses indicates the interaction between MHC proteins on the target cells with KIR2DL1 receptors on the NK cell. Figure 10 (unpublished data) presents a time-lapse interaction between a single YTS-KIR2DL1 cell (unlabeled) with five target cells (721.221/Cw6-GFP) forming four to five synapses. The upper panel (Figure 10a) indicates the morphology of the cells (bright field images) during the NK-target cell interaction (white arrows point out target cells). Figure 10b presents the accumulation of MHC/HLACw6-GFP proteins in the immune synapses at different time points (white arrows). Interestingly, we observed separation of the GFP protein accumulations on the immune synapses of two target cells, caused by the NK cell division into two daughter cells. The divided immune synapses where shown to be preserved between the two target cells and each NK daughter cell (Figure 10, t = 100 min, black arrows). The lower panel (Figure 10c) shows in false-color coding the green fluorescence from MHC/HLACw6-GFP clustering at the immune synapse. The divided synapses at t = 100 min are again highlighted with black arrows. Enhanced fluorescence is observed in other target cell sites besides the immune synapse. This can be explained by the heterogeneous GFP expression on target cells as well as by the different focal positions of target cells during imaging. The results in Figure 10 show that normal cellular functions such as immune synapse formation and mitosis are retained during the ultrasound exposure. These findings are in agreement with the conclusions drawn in Ref. [18].

Figure 10. Time-lapse recordings of the inhibitory interaction between a single NK cell (YTS KIR2DL cell line) and five target cells (721.221/Cw6-GFP). (**a**) Bright field image of the interaction indicating the morphology of the cells. White arrows point out the target cells. At t = 100 min the NK cell has divided into two NK cells; (**b**) Merged images of bright field and green channel indicating the accumulation of GFP protein (white arrows) in the interface between each target cell and the NK cell (the immune synapse). At t = 100 min, two of the synapses (of two target cells) are shown to have divided (black arrows) at the site of the NK cell division (GFP gap); (**c**) False-color coding of the green fluorescence clustering at the immune synapse. Again the divided synapses are highlighted with black arrows.

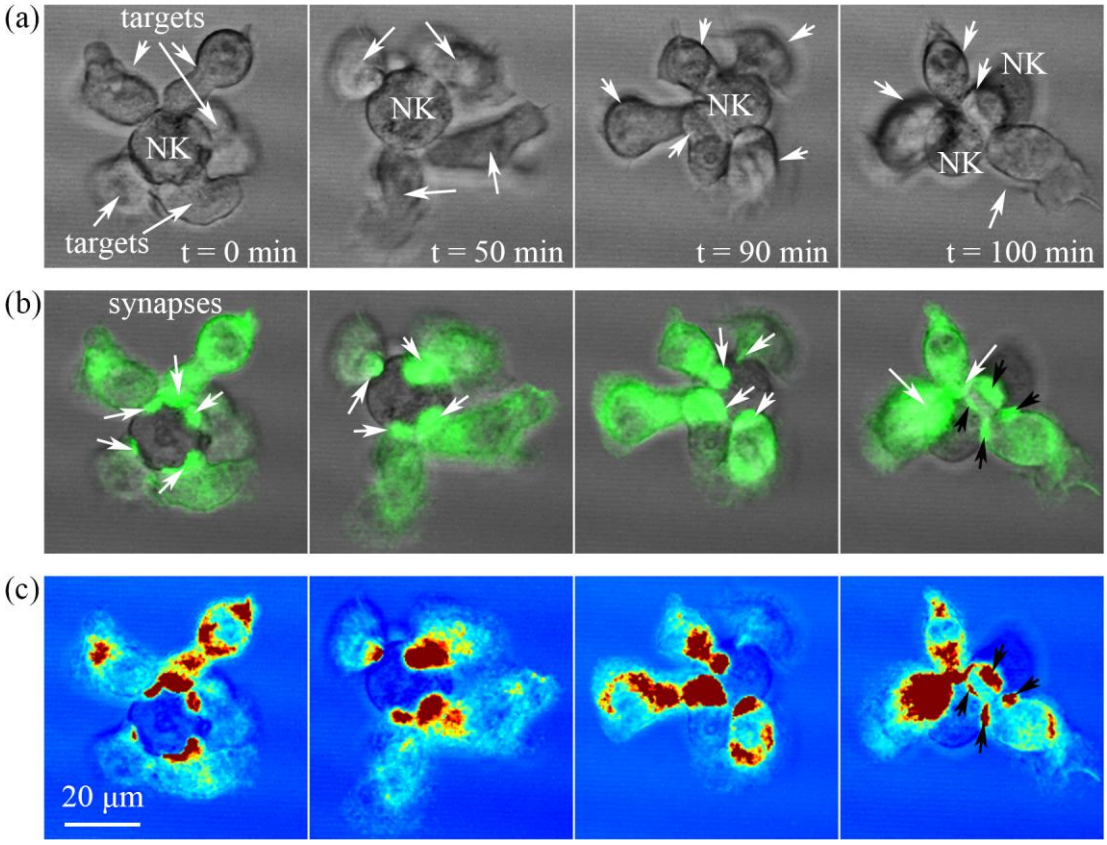

4.2. Studying the Killing Dynamics of Individual Natural Killer (NK) Cells

In the study by Christakou *et al*. [18], we characterized NK cells as cytotoxic effector cells by quantifying cytotoxic behaviors of individual NK cells against target cells. We performed several experiments in the multi-well microdevice using IL-2 activated polyclonal primary human NK cells isolated from lymphocyte enriched buffy coat residues derived from healthy donors. As target cells we used the 721.221 B cell line. We observed a significant heterogeneity in the natural killer cell population in their ability to induce cytotoxicity within a four hour assay of continuous contact with at least one target cell [18]. Analysis of four experiments (from two different donors) revealed that 64% of the NK cell population was able to kill at least one target cell, where the rest 36% remained non-cytotoxic during the entire experiment although in continues contact with one or more target cells. Interestingly, a small fraction of the NK cells showed a high killing performance eliminating all their surrounding target cells during the assay.

Figure 11. Time-lapse recordings of three parallel events among the 100 wells of the ultrasonic microplate in a 5 h cytotoxic assay. NK cells are shown in orange (orange calcein-AM), living target cells are shown in green (green calcein-AM) and dead target cells in red (far-red DDAO-SE). (**a**) Continuous interaction of a non-active NK cell (non-killer) with four to five targets (target cell division at t = 132 min) during the entire assay does not result to any NK cell mediated death; (**b**) Normal killer induces killing at t = 19 and 57 min, but remains inactive (although in contact with living target) for the remaining experiment; (**c**) Serial killer eliminating all four target cells within 75 min.

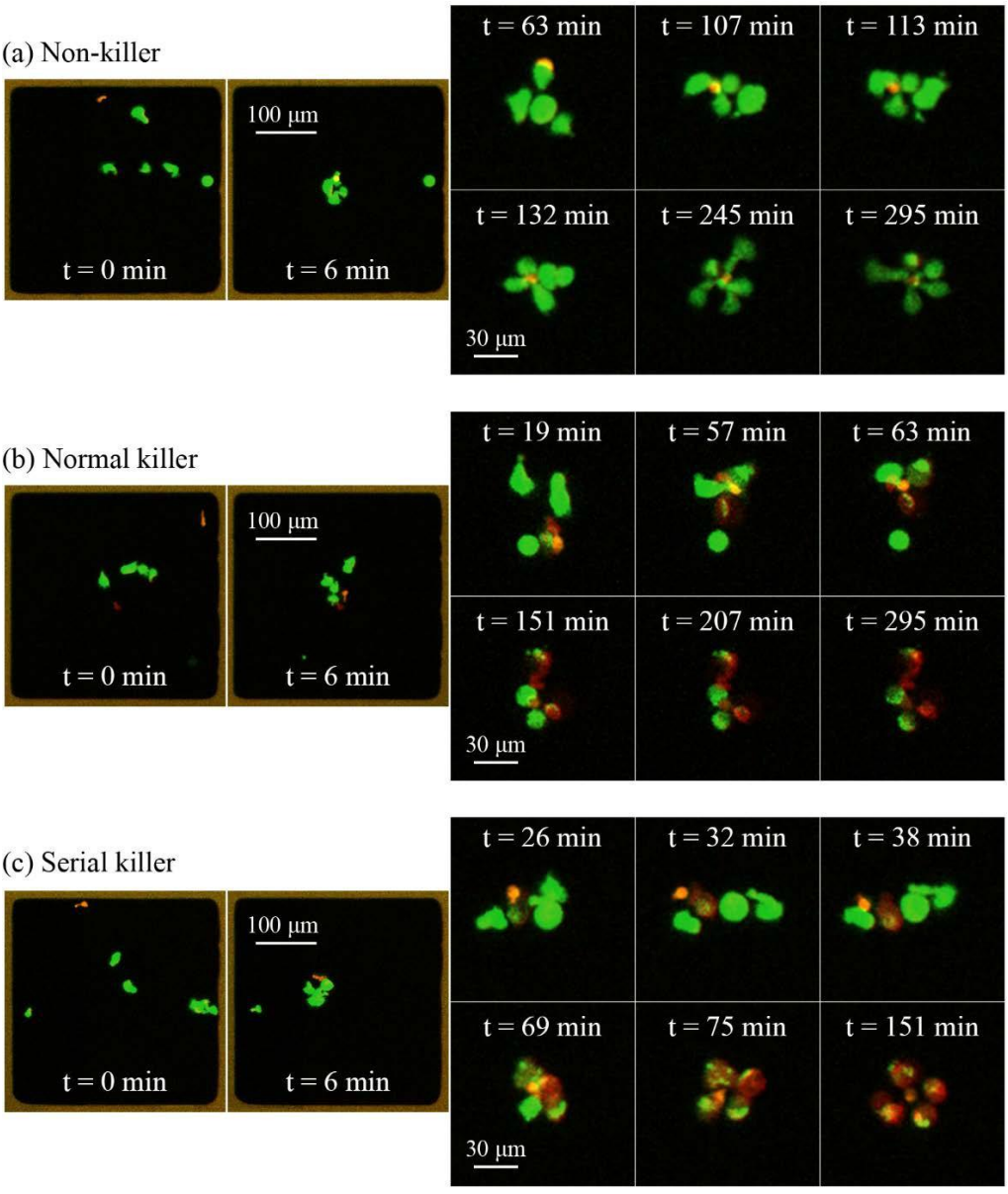

Time-lapse images of the three different NK cell killer types characterized by their cytotoxic abilities in a 5-h killing assay are exemplified in Figure 11. This is an equivalent experiment as reported in Ref. [18], but with one extra hour assay time. Here, NK cells were stained with orange calcein-AM while target cells were stained in a solution of green calcein-AM and Far red DDAO-SE. The property of calcein-AM to rapidly leak out when the cell membrane is raptured combined with increased DDAO intensity allows identification of cell death [7]. At t = 0 min, ultrasound was turned off and cells (NKs

and targets) are distributed in different positions in the wells. At t = 6 min ultrasound was turned on inducing NK-target cell contact. An inactive NK cell is presented in Figure 11a. Although it is in contact with several targets, it remained unable to induce death during the entire assay (at t = 295 min, green calcein-AM is still present in all target cells). A normal killer is presented in Figure 11b. The NK cell showed increased activity during the first hour (t = 57 min) of the assay killing two out of four target cells, but stayed inactive for the remaining 4 h (expected bleaching of the calcein-AM after long assays should not be confused with cell death). A serial killer, presented in Figure 11, eliminates all surrounding targets within only 75 min.

The property of some NK cells to rapidly kill targets cells is presented more detailed in Figure 12, where wells with individual NK cells and three or more target cells where analyzed and killing events, as well as the times of the killing events ($t_{death} - t_{contact}$, see Figure 9) where scored. Different colors indicate the number of kills induced by NK cells. Results indicate that NK cells, killing up to three target cells, show slower cytotoxic capability, killing every one to three hours, where some particular cells kill every 30 to 60 min eliminating most or all of their surrounding targets.

Figure 12. Timing of the killing events where the bars represent time from cluster formation until target cell death (mean and standard deviation for 1–3 kills). The different colors of the bars represent the order of the NK mediated target cell death within a cluster with red representing the first kills, blue the second, green the third, magenta the fourth, cyan the fifth, and yellow the sixth, respectively. The figure is reproduced from Ref. [18] with permission from RSC.

5. Conclusions

In this review, we have shown that ultrasound is a powerful and gentle tool for individual cell handling in a multi-well microplate. The described platform has been specifically designed for controlling cell-cell interactions, which are studied by high-resolution confocal and/or fluorescence microscopy. By distributing a few (typically 1–10) cells per well in a 100-well microplate, individual interactions can be monitored in real time and in parallel over time periods lasting for up to several days. The simple seeding method based on gravitational settlement allows for studying different constellations of interactions. For example, individual natural killer (NK) cells have been studied when interacting

simultaneously with different numbers of target cells. This made it possible to study the heterogeneity in cytotoxicity of NK cells, but also their ability to form one or several immune synapses simultaneously. Another strength of the platform is that ultrasound can be used not only for retaining an interaction and accurate positioning of the cell aggregate, but also for synchronizing the starting time of the cell–cell contacts in all 100 wells simultaneously. This made it possible to measure the time from the start of interaction to target cell death in a systematic and controlled way.

Of high importance is to evaluate any possible impact of the ultrasound exposure on the cell viability, proliferation rate and function. We have performed extensive measurements of these parameters over the last seven years. We have used different cell types, including animal cells and human cells, adherent cells and non-adherent cells, different cell lines and primary cells. The general conclusion made so far is that if ultrasound is driven in a controlled and well-calibrated manner (which primarily includes controlling the temperature and pressure amplitude at the employed actuation voltage and frequency), cells of various kinds can be continuously exposed to ultrasound for hours and even days without any noticeable effect on the studied parameters. Thus, we believe that our described platform may be of wide and general interest for any type of dynamic cell or cell–cell interaction study where a large number of cells need to be investigated in parallel and at the individual-cell level over extended periods in time.

Acknowledgments

We thank the Swedish Foundation for Strategic Research, the EU FP-7 RAPP-ID project, the Swedish Research Council, the Göran Gustafsson Foundation, the Jeansson Foundation, the Clas Groschinsky Foundation and the Åke Wiberg Foundation for financial support.

Conflicts of Interest

The authors declare no conflict of interest.

References

1. Single-Cell Analysis, Methods and Protocols. In *Methods in Molecular Biology*; Lindström, S., Andersson-Svahn, H., Eds.; Humana Press Inc.: New York, NY, USA, 2012.
2. Berridge, M.J.; Bootman, M.D.; Lipp, P. Calcium—A life and death signal. *Nature* **1998**, *395*, 645–648.
3. Pardee, A.B. G1 events and regulation of cell proliferation. *Science* **1989**, *246*, 603–608.
4. Ronowicz, E.; Coutinho, A. Functional analysis of B cell heterogeneity. *Immunol. Rev*. **1975**, *24*, 3–40.
5. Davey, H.M.; Kell, D.B. Flow cytometry and cell sorting of heterogeneous microbial populations: The importance of single-cell analyses. *Microbiol. Mol. Biol. Rev.* **1996**, *60*, 641–696.
6. Wiklund, M.; Brismar, H.; Önfelt, B. Acoustofluidics 18: Microscopy for acoustofluidic micro-devices. *Lab Chip* **2012**, *12*, 3221–3234.
7. Wiklund, M. Acoustofluidics 12: Biocompatibility and cell viability in microfluidic acoustic resonators. *Lab Chip* **2012**, *12*, 2018–2028.

8. Crowther, J.R. The ELISA Guidebook. In *Methods in Molecular Biology*; Humana Press Inc.: Totowa, NJ, USA, 2001.
9. Forslund, E.; Guldevall, K.; Olofsson, P.E.; Frisk, T.; Christakou, A.E.; Wiklund M.; Önfelt, B. Novel microchip-based tools facilitating live cell imaging and assessment of functional heterogeneity within NK cell populations. *Front. Immunol.* **2012**, *3*, 300; doi:10.3389/fimmu.2012.00300.
10. Lindström, S.; Larsson, R.; Andersson Svahn, H. Towards high-throughput single cell/clone cultivation and analysis. *Electrophoresis* **2008**, *29*, 1219–1227.
11. Guldevall, K.; Vanherberghen, B.; Frisk, T.; Hurtig, J.; Christakou, A.; Manneberg, O. Lindström, S.; Andersson-Svahn, H.; Wiklund, M.; Önfelt, B. Imaging immune surveillance of individual natural killer cells confined in microwell arrays. *PLoS One* **2010**, *5*, e15453; doi:10.1371/journal.pone.0015453.
12. Frisk, T.; Khorshidi, M.A.; Guldevall, K.; Vanherberghen, B.; Önfelt, B. A silicon-glass microwell platform for high-resolution imaging and high-content screening with single cell resolution. *Biomed. Microdevices* **2011**, *13*, 683–693.
13. Vanherberghen, B.; Olofsson, P.E.; Forslund, E.; Sternberg-Simon, M.; Khorshidi, M.A.; Pacouret, S.; Guldevall, K.; Enqvist, M.; Malmberg, K.-J.; Mehr, R.; *et al*. Classification of human natural killer cells based on migration behavior and cytotoxic response. *Blood* **2013**, *121*, 1326–1334.
14. Yamanaka, Y.J.; Berger, C.T.; Sips, M.; Cheney, P.C.; Alter, G.; Love, J.C. Single-cell analysis of the dynamics and functional outcomes of interactions between human natural killer cells and target cells. *Integr. Biol.* **2012**, *4*, 1175–1184.
15. Khorshidi, M.A.; Vanherberghen, B.; Kowalewski, J.M.; Garrod, K.R.; Lindström, S.; Andersson-Svahn, H.; Brismar, H.; Cahalan, M.D.; Önfelt, M. Analysis of transient migration behavior of natural killer cells imaged *in situ* and *in vitro*. *Integr. Biol.* **2011**, *3*, 770–778.
16. Vanherberghen, B.; Manneberg, O.; Christakou, A.; Frisk, T.; Ohlin, M.; Hertz, H.M.; Önfelt, B.; Wiklund, M. Ultrasound-controlled cell aggregation in a multi-well chip. *Lab Chip* **2010**, *10*, 2727–2732.
17. Ohlin, M.; Christakou, A.E.; Frisk, T.; Önfelt, B.; Wiklund, M. Influence of acoustic streaming on ultrasonic particle manipulation in a 100-well ring-transducer microplate. *J. Micromech. Microeng.* **2013**, *23*, 035008; doi:10.1088/0960-1317/23/3/035008.
18. Christakou, A.E.; Ohlin, M.; Vanherberghen, B.; Khorshidi, M.A.; Kadri, N.; Frisk, T.; Wiklund, M.; Önfelt, B. Live cell imaging in a micro-array of acoustic traps facilitates quantification of natural killer cell heterogeneity. *Integr. Biol.* **2013**, *5*, 712–719.
19. Lord Rayleigh. On the momentum and pressure of gaseous vibrations, and on the connexion with virial theorem. *Philos. Mag.* **1905**, *10*, 364–374.
20. Beyer, R.T. Radiation pressure—The history of a mislabeled tensor. *J. Acoust. Soc. Am.* **1978**, *63*, 1025–1030.
21. Gor'kov, L.P. On the forces acting on a small particle in an acoustical field in an ideal fluid. *Sov. Phys. Dokl.* **1962**, *6*, 773–775.
22. Manneberg, O.; Svennebring, J.; Hertz, H.M.; Wiklund, M. Wedge transducer design for two-dimensional ultrasonic manipulation in a microfluidic chip. *J. Micromech. Microeng.* **2008**, *18*, 095025; doi:10.1088/0960-1317/18/9/095025.

23. Nyborg, W.L. Theoretical criterion for acoustic aggregation. *Ultrasound Med. Biol.* **1989**, *15*, 93–99.
24. Manneberg, O.; Vanherberghen, B.; Svennebring, J.; Hertz, H.M.; Önfelt, B.; Wiklund, M. A three-dimensional ultrasonic cage for characterization of individual cells. *Appl. Phys. Lett.* **2008**, *93*, 063901; doi:10.1063/1.2971030.
25. Barnkob, R.; Augustsson, P.; Magnusson, C.; Lilja, H.; Laurell, T.; Bruus, H. Measuring Density and Compressibility of White Blood Cells and Prostate Cancer Cells by Microchannel Acoustophoresis. In Proceedings of the 15th MicroTAS, Seattle, WA, USA, 2–6 October 2011.
26. Hartono, D.; Liu, Y.; Tan, P.L.; Then, X.Y.S.; Yung, L.Y.L.; Lim, K.M. On-chip measurements of cell compressibility via acoustic radiation. *Lab Chip* **2011**, *11*, 4072–4080.
27. Mishra, P.; Glynne-Jones, P.; Boltryk, R.J.; Hill, M. Efficient finite element modeling of acoustic radiation forces on inhomogeneous elastic particles. *AIP Conf. Proc.* **2012**, *1433*, 753–756.
28. Iranmanesh, I.; Barnkob, R.; Bruus, H.; Wiklund, M. Tunable-angle wedge transducer for improved acoustophoretic control in a microfluidic chip. *J. Micromech. Microeng.* **2013**, *23*, 105002; doi:10.1088/0960-1317/23/10/105002.
29. Bruus, H. Acoustofluidics 2: Perturbation theory and ultrasound resonance modes. *Lab Chip* **2012**, *12*, 20–28.
30. Wiklund, M.; Green, R.; Ohlin, M. Acoustofluidics 14: Applications of acoustic streaming in microfluidic devices. *Lab Chip* **2012**, *12*, 2438–2451.
31. Ohlin, M.; Christakou, A.E.; Frisk, T.; Önfelt, B.; Wiklund, M. Controlling Acoustic Streaming in a Multi-well Microplate for Improving Live Cell Assays. In Proceedings of the 15th International Conference on Miniaturized Systems for Chemistry and Life, Sciences (MicroTAS 2011), Seattle, WA, USA, 2–6 October 2011.
32. Barnkob, R.; Iranmanesh, I.; Wiklund, M.; Bruus, H. Measuring acoustic energy density in microchannel acoustophoresis using a simple and rapid light-intensity method. *Lab Chip* **2012**, *12*, 2337–2344.
33. Barnkob, R.; Augustsson, P.; Laurell, T.; Bruus, H. Measuring the local pressure amplitude in microchannel acoustophoresis. *Lab Chip* **2010**, *10*, 563–570.
34. Hultström, J.; Manneberg, O.; Dopf, K.; Hertz, H.M.; Brismar, H.; Wiklund, M. Proliferation and viability of adherent cells manipulated by standing-wave ultrasound in a microfluidic chip. *Ultrasound Med. Biol.* **2007**, *33*, 145–151.
35. Raffel, M.; Willert, C.E.; Wereley, S.T.; Kompenhans, J. *Particle Image Velocimetry*; Springer: Berlin, Germany, 2007.
36. Augustsson, P.; Barnkob, R.; Wereley, S.T.; Bruus, H.; Laurell, T. Automated and temperature-controlled micro-PIV measurements enabling long-term-stable microchannel acoustophoresis characterization. *Lab Chip* **2011**, *11*, 4152–4164.
37. Barnkob, R.; Augustsson, P.; Laurell, T.; Bruus, H. Acoustic radiation- and streaming-induced microparticle velocities determined by microparticle image velocimetry in an ultrasound symmetry plane. *Phys. Rev. E* **2012**, *86*, 056307; doi:10.1103/PhysRevE.86.056307.
38. Apfel, R.E.; Holland, C.K. Gauging the likelihood of cavitation from short-pulse, low-duty cycle diagnostic ultrasound. *Ultrasound Med. Biol.* **1991**, *17*, 179–185.

39. Augustsson, P.; Magnusson, C.; Nordin, M.; Lilja, H.; Laurell, T. Microfluidic, label-free enrichment of prostate cancer cells in blood based on acoustophoresis. *Anal. Chem*. **2012**, *84*, 7954–7962.
40. Burguillos, M.A.; Magnusson, C.; Nordin, M.; Lenshof, A.; Augustsson, P.; Hansson, M.J.; Elmér, E.; Lilja, H.; Brundin, P.; Laurell T.; Deierborg, T. Microchannel acoustophoresis does not impact survival or function of microglia, leukocytes or tumor cells. *PLoS One* **2013**, *8*, e64233; doi:10.1371/journal.pone.0064233.
41. Bazou, D. Biochemical properties of encapsulated high-density 3-D HepG2 aggregates formed in an ultrasound trap for application in hepatotoxicity studies. *Cell Biol. Toxicol.* **2010**, *26*, 127–141.
42. Orange, J. Formation and function of the lytic NK-cell immunological synapse. *Nat. Rev. Immunol.* **2008**, *8*, 713–725.
43. Monks, C.R.; Freiberg, B.A.; Kupfer, H.; Sciaky, N.; Kupfer, A. Three-dimensional segregation of supramolecular activation clusters in T cells. *Nature* **1998**, *395*, 82–86.
44. Grakoui, A.; Bromley, S.K.; Sumen, C.; Davis, M.M.; Shaw, A.S.; Allen, P.M.; Dustin, M.L. The immunological synapse: A molecular machine controlling T cell activation. *Science* **1999**, *285*, 221–227.
45. Ljunggren, H.-G.; Kärre, K. In search of the "missing self": MHC molecules and NK cell recognition. *Immunol. Today* **1990**, *11*, 237–244.
46. Bhat, R.; Watzl, C. Serial killing of tumor cells by human natural killer cells—Enhancement by therapeutic antibodies. *PLoS One* **2007**, *2*, e326; doi:10.1371/journal.pone.0000326.
47. Yawata, M.; Yawata, N.; Draghi, M.; Partheniou, F.; Little, A.-M.; Parham, P. MHC class I-specific inhibitory receptors and their ligands structure diverse human NK-cell repertoires toward a balance of missing self-response. *Blood* **2008**, *112*, 2369–2380.
48. Brodin, P.; Lakshmikanth, T.; Johansson, S.; Kärre, K.; Höglund, P. The strength of inhibitory input during education quantitatively tunes the functional responsiveness of individual natural killer cells. *Blood* **2009**, *113*, 2434–2441.